Measurement of multiple scattering of 13 and 20 MeV electrons by thin foils

C. K. Ross,[a] M. R. McEwen, A. F. McDonald,[b] and C. D. Cojocaru
Ionizing Radiation Standards, Institute for National Measurement Standards, National Research Council, Ottawa, Ontario K1A 0R6, Canada

B. A. Faddegon
Department of Radiation Oncology, University of California San Francisco, California 94143-1708

(Received 4 February 2008; revised 19 June 2008; accepted for publication 16 July 2008; published 18 August 2008)

To model the transport of electrons through material requires knowledge of how the electrons lose energy and scatter. Theoretical models are used to describe electron energy loss and scatter and these models are supported by a limited amount of measured data. The purpose of this work was to obtain additional data that can be used to test models of electron scattering. Measurements were carried out using 13 and 20 MeV pencil beams of electrons produced by the National Research Council of Canada research accelerator. The electron fluence was measured at several angular positions from 0° to 9° for scattering foils of different thicknesses and with atomic numbers ranging from 4 to 79. The angle, $\theta_{1/e}$, at which the fluence has decreased to $1/e$ of its value on the central axis was used to characterize the distributions. Measured values of $\theta_{1/e}$ ranged from 1.5° to 8° with a typical uncertainty of about 1%. Distributions calculated using the EGSnrc Monte Carlo code were compared to the measured distributions. In general, the calculated distributions are narrower than the measured ones. Typically, the difference between the measured and calculated values of $\theta_{1/e}$ is about 1.5%, with the maximum difference being 4%. The measured and calculated distributions are related through a simple scaling of the angle, indicating that they have the same shape. No significant trends with atomic number were observed. [DOI: 10.1118/1.2968095]

Key words: electron scattering, multiple scattering, scattering power

I. INTRODUCTION

Monte Carlo techniques are used widely to study the transport of ionizing radiation through matter. Recent review articles on the use of Monte Carlo in medical physics are available in a handbook edited by Mayles *et al.*[1]

Electron transport is complicated because of the large number of interactions an individual electron will undergo before coming to rest. Even with present-day computer systems, for most problems, it is not practical to model every electron interaction so condensed history techniques are used.[2] Electron energy loss is characterized by the stopping power[3] which is obtained from a theoretical model that is supported by a limited amount of experimental data. In addition to losing energy, largely through interactions with the atomic electrons, electrons are also scattered elastically by the atomic nuclei. Just as energy loss is characterized by a stopping power, electron scattering can be characterized by a scattering power.[4] However, the scattering power only specifies the change in the mean square scattering angle per unit thickness of material so plays no direct role in Monte Carlo simulations. Instead, the distribution of scattered electrons is obtained from a theoretical model, such as that of Molière.[5]

There are only a limited number of measurements that directly test the calculated angular distribution of scattered electrons. Perhaps the most accurate data are those of Hanson *et al.*[6] for 15.7 MeV electrons. Their data have been compared to the predictions of the EGS4 Monte Carlo code by Li and Rogers[7] and to several other popular codes by Vilches *et al.*[8–10] Additional data for electrons have been reported by Kulchitsky and Latyshev[11] (2.25 MeV), by Heymann and Jennings,[12] (4.5 MeV) and by Kovalev *et al.*[13] (12–25 MeV).

The EGS4 (Ref. 14) and EGSnrc (Ref. 15) Monte Carlo codes are widely used for studying problems in medical physics. The simulation of electron multiple scattering in EGS4 is based on the multiple scattering theory of Molière. The approximations inherent in Molière's theory have been extensively studied by several authors, including Bethe,[16] Bielajew,[17] and Fernández-Varea *et al.*[18] Andreo *et al.*[19] show that some of the numerical approximations inherent in the model can lead to errors of up to 6%. Kawrakow and Bielajew[20] developed a more accurate multiple scattering theory based on the work of Goudsmit and Saunderson, and Kawrakow[15] implemented this approach in EGSnrc.

Faddegon *et al.*[21] compare measured absorbed dose to water distributions with distributions calculated using the EGSnrc and GEANT4 Monte Carlo codes. By varying the electron beam characteristics and the treatment head geometry, they find that both codes can reproduce the measured data. Although the variations introduced are plausible, it is not known if they accurately describe the accelerator or compensate for inadequacies in the Monte Carlo codes. The authors draw attention to the need for better benchmark data with no free parameters.

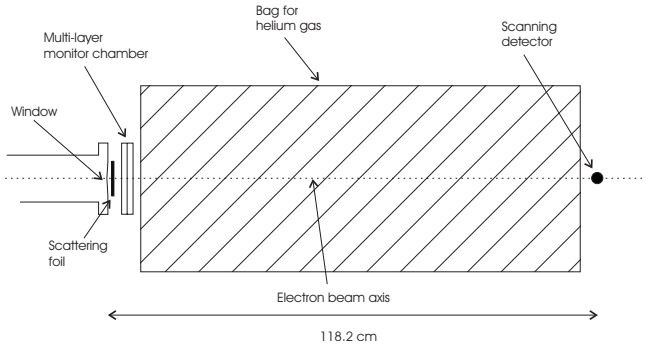

FIG. 1. Overview of the apparatus used to measure electron scattering distributions. The detector was located 118.2 cm from the beam exit window and was mounted on a linear translator. Distributions were measured with helium gas in the space between the monitor chamber and detector. A thin cylindrical Mylar bag was used to contain the helium gas. Except for the helium bag, all components can be considered to be of infinite extent in the transverse direction.

The recent articles by Vilches *et al.*[8–10] compare the results of several Monte Carlo codes to the best experimental data. Their work shows that the different codes predict differences of more than 20% for the widths of the scatter distributions and the authors stress the need for additional experimental data.

The objective of this work is to provide additional measured data for electron scattering distributions for scattering foils spanning a range of thicknesses and atomic numbers. The scatter geometry and the electron beam are well characterized, with no free parameters. We compare our measured data to the predictions of the EGSnrc Monte Carlo code. We also use the code to estimate corrections and possible systematic effects that would otherwise be difficult to evaluate or would require a considerably more sophisticated apparatus to eliminate.

II. MATERIALS AND METHODS

II.A. Overview

Figure 1 is a schematic diagram of the key components of the apparatus. A pencil beam of electrons passed through a thin exit window that is described in more detail in Sec. II C. The beam impinged on a scattering foil and then passed through a transmission monitor chamber. The scattered electron beam passed through helium at atmospheric pressure and was measured 118.2 cm downstream of the exit window. The detector was mounted on a linear positioning system that allowed it to be scanned across the scattered electron beam. Measurements could be made at scattering angles of up to 9° on either side of the beam axis. The distance from the exit window to the scattering foil was 28 mm and from the exit window to the center of the monitor chamber 50 mm. The Mylar® bag was 110 cm long. Note that all components except the helium bag can be considered to be of infinite extent in the transverse plane.

II.B. Electron beam characteristics

The electron beam was produced by the National Research Council of Canada (NRC) Vickers linear accelerator operating at a pulse repetition rate of 240 Hz and a pulse width of about 2.5 μs. This accelerator produces a horizontal beam of electrons which is transported for several meters through an evacuated drift tube to the exit window. Magnets along the transport path are used to establish the electron energy as well as to focus and steer the beam. The beam position and focus were observed using a profile monitor located 10 cm upstream of the exit window. The beam axis downstream of the exit window was identified by a laser beam. In order to align the electron beam so that it was coincident with the laser beam a quadrant ionization chamber was set up at a distance of about 120 cm. An x-ray target was placed near the exit window and the x-ray signal from the quadrant ionization chamber combined with the electron beam position indicated by the profile monitor were used to adjust the beam steering. An x-ray beam was used rather than the primary electron beam in order to match the sensitivities of the profile monitor and the quadrant ionization chamber. Once the beam was aligned, the x-ray target and ionization chamber were removed, and the electron current adjusted to about 7 nA. This current was sufficient to give an absorbed dose rate to water of about 20 Gy/min at the detector position with no scattering foil in place.

The electron beam energy was defined by a bending magnet and slit system, and the calibration of this system was established using a magnetic spectrometer.[22] The estimated standard uncertainty on the electron energy is 0.4%. The energy distribution was approximately Gaussian in shape with a standard deviation of 0.4%.

The beam profile monitor indicated that the beam profile also was approximately Gaussian in shape with a full width at half maximum (FWHM) of less than 2 mm. More detailed profile measurements were made using Far West radiochromic film (Far West Technology, Inc., Goleta, CA, USA). Pieces of FWT-60 film, 2 cm square, were mounted on the beam exit window and irradiated so that the maximum net absorbance was about 0.9. The absorbance, which is proportional to absorbed dose, was read using a spectrophotometer equipped with a scanner for moving the film in a plane at right angles to the light beam. An aperture restricted the light beam to 0.5 mm and the scanner was moved in steps of 0.2 mm. The results are summarized in the left-hand panels of Fig. 2 and show that the electron beam at the focal point does not have exact cylindrical symmetry but the FWHM is approximately 1 mm.

In order to measure the angular divergence of the beam, the standard beam exit flange and window were removed and an extra 1 m piece of drift pipe with a thin exit window at the end was added to the beam line. Again, pieces of FWT-60 film were irradiated on the exit window and the absorbance profiles measured. The results are shown in the right panels of Fig. 2 and show that, although the beam diverges somewhat in drifting 1 m, the main feature is a secondary lobe of about one-third the intensity of the primary beam. The situ-

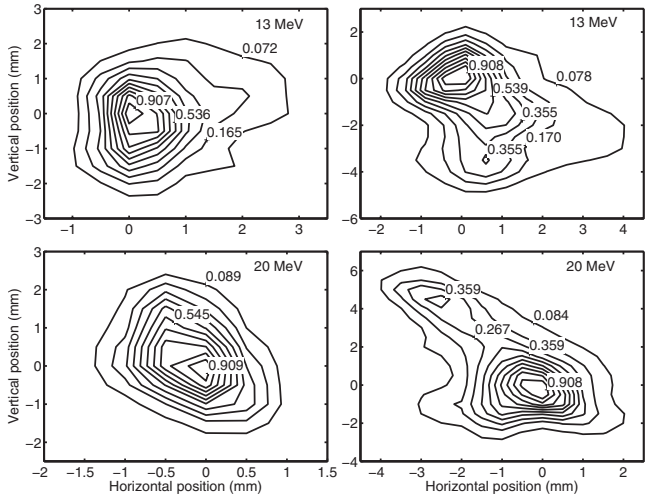

FIG. 2. Electron beam profiles measured using radiochromic film. The left-hand panels show the distribution measured at the standard beam exit window, while those on the right give the profiles after the beam has drifted in vacuum an additional 1 m. The intervals between contours are equal but only a few are labeled. The contours are labeled according to the absorbance measured at 605 nm.

ation is similar for the two energies, with the secondary lobe diverging from the primary beam with an angle of between 0.2° and 0.25°. The effect of these beam characteristics on the measured distributions is assessed in Sec. III B.

II.C. Scattering foils

The key properties of the scattering foils used are given in Table I. The mass thickness of each foil was obtained by assuming it was of uniform thickness and calculating the ratio of the mass to the surface area. Foil thicknesses ranged from 5 mm for Be to 16 μm for Au. Some of the foils were closely circular with a diameter of 5 cm. Others were approximately square with sides of 2 cm. For the thick circular foils, the diameter was measured using digital calipers. In other cases, the foil was photographed using a digital camera and ImageJ software[28] used to determine the area. The foil mass was obtained using a balance with a resolution of 10 μg.

The exit window of the accelerator beam line is made from a titanium alloy identified as Ti90/Al6/V4, where the numbers give the percentage by weight of the elements Ti, Al, and V. Additional thicknesses of this foil were also used as scattering material.

Although not intended as such, the transmission monitor chamber also acted as a composite scattering foil. This chamber is from an Elekta medical accelerator and is composed of six foils. The diameter of each foil is about 9 cm and the distance between the first and last is 6 mm. Each foil is Mylar, 12 μm thick, coated on one side with a 12 μm thick layer of a graphite-based conductive ink with an approximate density of 1 g/cm^3. Charge from one of its air cavities was used to monitor and control the accelerator while a second was used to normalize the detector reading.

II.D. Detectors

Scattered electron distributions were measured with both ionization chamber and diode detectors. The point of measurement was taken to be at the center of the sensitive volume of the detector. Ionization chambers included an Exradin A16, a PTW 233642 and an Exradin A2. Diode detectors included the electron (EFD) and stereotatic (SFD) diodes manufactured by Scanditronix and the PTW 60012 electron diode.

Each detector was mounted on a stand attached to a Velmex linear translator with an available travel of 130 cm. The translator was positioned at right angles to the beam and centered so that the detector could be moved the same distance on either side of the central axis.

The output currents from the monitor chamber and moveable detector were read by Keithley electrometers that were connected to a personal computer. The translator was also computer controlled so that the detector could be moved to a

TABLE I. Summary of the key characteristics of the scattering foils. The mass thickness was obtained by weighing each foil and measuring its surface area. Typically, several different foils were used, as indicated by the four columns on the right of the table. Except for the first Cu foil, the foils of a given material were considered equivalent. For the electron scattering measurements the total scattering foil thickness was made up of one or more of the individual foils. Carbon (C) was in the form of pyrolytic graphite.

Foil material	Z	Tabulated density (g/cm^3)	Measured foil thickness (mg/cm^2)			
Ti alloy	—	4.42	18.24	17.97	18.30	18.31
Be	4	1.85	926	—	—	—
C	6	2.18	546	—	—	—
Al	13	2.70	69.91	69.73	70.52	—
Cu	29	8.92	44.92	43.25	43.40	42.96
Ta	73	16.65	44.3	206.3	—	—
Au	79	19.30	31.10	31.52	30.99	31.36
Au	79	19.30	54.48	55.51	54.40	54.59

given position, the charge collected for a preset time from both the monitor and detector, and the process repeated until the data for a complete scan was collected.

II.E. He gas column

Using the scattering power data tabulated in ICRU 35, one can estimate the effect of a 1 m air column on the scattered distribution produced by the beam exit window. For 20 MeV electrons the mean-square scattering angle, $\langle\theta^2\rangle$, due to the window is 9.6×10^{-4} rad^2 ($\sqrt{\langle\theta^2\rangle}=1.8°$) while for a 1 m air column it is 2.6×10^{-3} rad^2 (2.9°). On the other hand, for a 1 m column of helium gas $\langle\theta^2\rangle$ is 1.0×10^{-4} rad^2 (0.6°). Because of the significant scattering produced by the air column and because of the significant reduction possible by replacing the air with helium, a container was constructed that would permit most of the air between the window and detector to be replaced with helium.

Two aluminum rings, with an inner diameter of 40 cm, formed the ends of the bag and were held in place with a low-mass support. Aluminized Mylar, comprised of Mylar foil 25 μm thick and coated on one side with approximately 24 nm of aluminum, was used to form the cylindrical side wall and planar end walls of the gas bag. An oxygen monitor was used to measure the presence of oxygen in the beg. To initially purge the bag of air, several venting holes were opened and a fairly high flow rate of helium maintained. After about 30 min, the oxygen concentration was close to zero at which time all of the venting holes except one was closed. From then on, a modest flow of helium maintained the oxygen concentration close to zero. The helium exited the bag through a rubber tube which was immersed in a few millimeters of water. At this depth a constant flow of bubbles was observed, but placing the tube at a depth of about 1 cm stopped the flow. Thus, we estimate that the helium gas in the bag was within about 0.1% of atmospheric pressure.

II.F. Monte Carlo codes

All simulations were done using the EGSnrc Monte Carlo code[15,23] and its associated user codes, including BEAMnrc (Ref. 24) and `cavity`.[25] In addition to being used to compare measured and calculated scatter distributions, EGSnrc and its user codes were used to estimate correction factors that were needed in the analysis of the measured data.

II.G. Measuring scatter distributions

For each scattering foil configuration the detector was scanned symmetrically with respect to the axis defined by the laser beam. We use the angle formed by the beam axis and the ray intersecting the beam axis at the exit window and passing through the center of the detector to describe the detector position. Figure 3 shows the scatter distributions obtained with no added scattering foil and with an additional 36.4 mg/cm^2 of Ti alloy. Because the effect of ion recombination in the monitor chamber was very large and depended on which scattering foil was in place, we were not able to establish the relative fluence rates between different scattering geometries so all measured distributions are normalized to unity on the central axis.

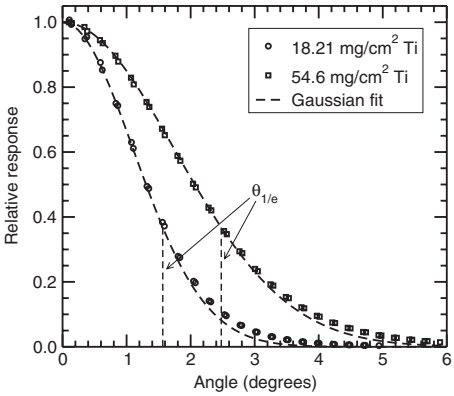

FIG. 3. Typical measured scatter distributions for 20 MeV electrons and scattering foils of Ti alloy. Also shown are Gaussian fits to the data. The vertical dashed lines show the values of $\theta_{1/e}$ used to generate the Gaussian fits. Because these are the uncorrected values of $\theta_{1/e}$, they differ slightly from the values given in Table III.

Typically, the peak of the fluence distribution at the detector position coincided with the beam axis to better than 3 mm. The alignment of the electron beam in the vertical direction was checked from time to time using a separate linear translator. Differences between the actual and ideal beam positions were similar to those observed for horizontal scans. Beam alignment is most important for the narrowest distributions. Using a two-Gaussian approximation to the scatter distribution obtained with no added scattering foils one can show that a misalignment of 5 mm increases $\theta_{1/e}$, the angle at which the distribution has fallen to $1/e$ of its value on the central axis, by 0.3%. This result is consistent with the measured value obtained by intentionally offsetting the detector position in the vertical direction.

The detector background was measured with the electron beam off and the detector stationary. If significant, the background was subtracted and the measured distribution reflected about its symmetry axis. The distribution was also corrected for dose rate or ion recombination effects, if significant. The largest effect on $\theta_{1/e}$ was 1.6% and 0.4% for dose rate and ion recombination, respectively. The typical results presented in Fig. 3 confirm the well-known fact[4] that a Gaussian distribution fits the central portion of the scatter distribution but cannot fit the complete distribution. Nevertheless, $\theta_{1/e}$ is a useful parameter for characterizing the general features of the scatter distributions and we will use it for that purpose. We determined $\theta_{1/e}$ by fitting the square of the scattering angle versus the negative of the natural logarithm of the amplitude of the distribution, normalized to unity on the central axis, $[-\ln(I/I_0)]$, to a straight line. In general, all data for which $-\ln(I/I_0)\leq1$ were used for the fit. However, points close to, but slightly larger than, unity were also included.

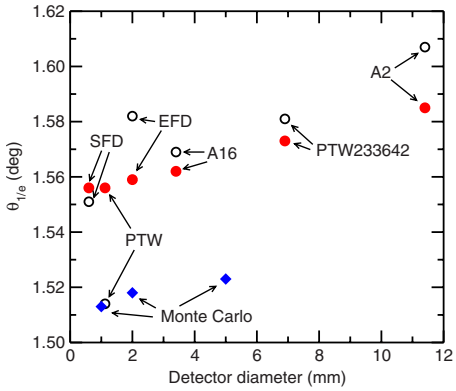

FIG. 4. Apparent width of the measured scatter distribution as a function of the size of the detector. The distribution was produced by 20 MeV electrons with no added scattering foils. Open circles: results obtained with no corrections to the detector response. Closed circles: results after the ionization chamber response has been corrected for ion recombination and the diode response for dose rate effects. Filled diamonds: results for the calculated scatter distribution for voxel sizes from 1 to 5 mm.

TABLE II. Comparison of the values of $\theta_{1/e}$ measured by Hanson *et al.* (Ref. 6) with the values we calculated using EGSnrc. We also include the differences reported by Vilches *et al.* (Ref. 8) for EGSnrc. (Although these values were not reported in tabular form by Vilches *et al.*, they could be read off a graph in their article.) The second row for each Au foil corresponds to the results obtained when we refit the Hanson *et al.* data using the same procedure as we used for fitting the Monte Carlo data. (Vilches *et al.* report 2.50° and 3.71° for the Au foils using their fitting procedure.)

				Difference	
	Thick. (mg/cm^2)	Meas. (deg)	Calc. (deg)	NRC (%)	Vilches *et al.* (Ref. 8) (%)
Be	257	3.06	3.00	−2.0	0
	495	4.25	4.40	3.5	5.1
Au	18.66	2.58	2.44	−5.4	—
	18.66	2.48	2.44	−1.6	−1.8
	37.28	3.76	3.75	−0.3	—
	37.28	3.71	3.75	1.1	0.9

II.H. Calculating scatter distributions

Although the primary motivation for this work was to provide benchmark data that can be used to test calculations, we also compared our measured results with the predictions of the EGSnrc Monte Carlo package and its associated user codes. The BEAMnrc code was used to simulate the measurement geometry as illustrated in Fig. 1. The incident electron beam was taken to be monoenergetic with an intensity profile that was Gaussian in shape with a root mean-square radius of 1 mm. The beam angular spread and its effect on the measured distributions is discussed in Sec. III B. EGSnrc user code DOSXYZnrc was used to score the absorbed dose to water in cubic voxels, 5 mm on a side, on a plane at right angles to the beam axis and 118.2 cm downstream of the beam exit window. The absorbed dose in a thin layer of water or similar material is expected to be proportional to the electron fluence impinging on the surface. This assumption was tested by using BEAMDP (Ref. 26) to score the electron fluence for the case with no added scattering foil. Both techniques gave the same value for $\theta_{1/e}$. We also used `cavity` to create a realistic simulation of the Exradin A16 ionization chamber in air and calculated the ionization response as a function of chamber position. This approach also produced a scatter distribution in excellent agreement with those from DOSXYZnrc and BEAMDP. Because we needed to investigate the effects of asymmetries in the incident beam, we could not assume cylindrical symmetry and hence chose to use DOSXYZnrc for calculating all of the scatter distributions.

A separate study of the effect of voxel size on the apparent width of the calculated distribution was carried out. The results are summarized in Fig. 4 and show that changing the voxel size from 5 to 1 mm changed $\theta_{1/e}$ for the narrowest distribution by about 0.7%.

The foils of Ti alloy were simulated using the true elemental composition, not as pure Ti. The monitor chamber was simulated as a single foil of Mylar having the same mass thickness as the actual chamber. All other scattering foils were assumed to be without significant impurities. The diameter of the helium bag (46 cm) defined the maximum radial extent for the simulation geometry. Circular symmetry was assumed and air filled all of the simulation geometry not otherwise assigned to some material. The radial dimensions assigned to the components are given in the Appendix.

EGSnrc radiation transport parameters are discussed by Kawrakow.[15] The values used for this work included electron lower energy cutoffs ECUT and AE of 0.7 MeV, and photon lower energy cutoffs PCUT and AP of 10 keV. The boundary-crossing algorithm (BCA) was set to EXACT (single scattering). The electron-step algorithm was set to PRESTA-II. Other parameters included a maximum step size SMAX of 5 cm, ESTEPE of 0.25, XIMAX of 0.5, skin depth for BCA defaulted, spin effect on, bremsstrahlung angular sampling set to Simple, pair angular sampling set to Simple, and bremsstrahlung cross section set to Bethe-Heitler. Bound Compton scattering, Rayleigh scattering, atomic relaxations, and photoelectron angular sampling were all turned off. BEAMnrc was run as a shared library, thus eliminating the need to save phase-space files or to recycle phase-space data. Typically 10^8 electron histories were followed and required about 9 h when run on a 1.8 GHz processor.

To confirm that our Monte Carlo calculations are consistent with results in the literature, we calculated the distributions expected for the scattering foils used by Hanson *et al.*[6] The comparison is shown in Table II along with the EGSnrc Monte Carlo values reported by Vilches *et al.*[8] Our result for the thinner gold foil differs by more than 5% from the values of $\theta_{1/e}$ reported by Hanson *et al.* However, Vilches *et al.* have refit the Au data of Hanson *et al.* using the same numerical procedure they used to analyze their calculated data and obtain a value for the thinner Au foil that is more than 3% different than the Hanson *et al.* value. When we refit the Hanson *et al.* data we obtain a similar result and our EGSnrc Monte Carlo values for the gold foils agree within 0.2% with those of Vilches *et al.* Hanson *et al.* do not provide detailed scatter distributions for Be so we cannot refit their data to

obtain $\theta_{1/e}$. The differences between our EGSnrc calculations and their tabulated values of $\theta_{1/e}$ for Be are similar to the differences for Au. More surprising is that the agreement between our calculations and those of Vilches *et al.* for Be is not as good as for Au, with our EGSnrc calculations predicting distributions that are narrower than those of Vilches *et al.* by about 2%.

Although Hanson *et al.* do not give uncertainty estimates, the scatter of their data suggests that the differences between the measured and calculated distributions for the gold foils are not statistically significant. The larger differences for Be may be due to the fact that we do not have access to the full scatter distributions and so cannot use a consistent approach for extracting $\theta_{1/e}$. We would expect the two EGSnrc Monte Carlo calculations to be in close agreement, and they are for Au, but they differ by 2% for Be. Despite this discrepancy the agreement for the gold foils gives us confidence to compare our Monte Carlo calculations with the new experimental data.

III. RESULTS AND DISCUSSION

III.A. Detector response

For this work, an ideal detector would have negligible size, show no response to photons, and have a response to electrons that does not depend on energy or fluence rate. The characteristic angle $\theta_{1/e}$ for the narrowest distribution we measured is about 1.5°. Using Gaussian approximations, a detector with a spatial resolution of 5 mm would be expected to broaden this distribution by about 0.005°, or 0.3%. We measured the apparent width of the scattered electron distribution for 20 MeV electrons with no added foils using all of the detectors considered for this study. The results are shown in Fig. 4, where $\theta_{1/e}$ is plotted against the diameter of the detector. The open symbols do not show a consistent trend, but there are two effects that must be considered. Because the absorbed dose rate varies by as much as a factor of 10 over the scatter distribution, ion recombination may affect the results obtained using ionization chambers while changes in the response with dose rate may affect the results obtained with diodes. An independent study at NRC showed that the dose rate effect is particularly large for the PTW diode, with its response increasing as the dose rate increases. When the data are corrected for ion recombination and dose rate, the results shown by the solid symbols are obtained. Now the data show a consistent trend with detector size, and the distribution broadening is consistent with expectations. All of the results reported here were obtained with either the A16 ionization chamber or the EFD diode. Combined with the Monte Carlo results reported in Sec. II H, we conclude that Monte Carlo calculations using 5 mm voxels can be compared with measurements obtained using the EFD diode or the A16 ionization chamber without any corrections for resolution broadening.

In order to estimate the bremsstrahlung contribution to the detector response, the helium bag was removed and an electromagnet was placed immediately downstream of the monitor chamber.

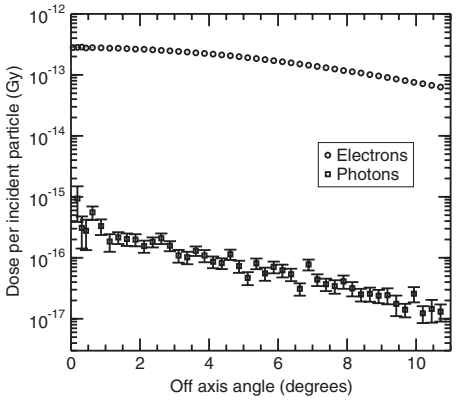

FIG. 5. Contributions of electrons and photons to the absorbed dose to water at the detector position. The results were calculated using EGSnrc and are for 20 MeV electrons impinging on a Au gold scattering foil, 220 mg/cm^2 thick.

With the magnet energized, the electron scatter distribution could be swept away from the central axis leaving only the bremsstrahlung component. Because of large-angle scattering, the electron contribution could not be completely eliminated, even for thin scattering foils. However, by comparing standard and offset distributions we could estimate the maximum bremsstrahlung contribution. For 20 MeV electrons on a Au foil 219 mg/cm^2 thick, this approach provides an upper limit on the bremsstrahlung contribution of less than 0.2%.

We also used the EGSnrc code to calculate the bremsstrahlung contribution by scoring the absorbed dose in a slab of water 2 mm thick. The maximum effect is expected for 20 MeV electrons on the thickest gold foil and Fig. 5 shows the separate contributions of electrons and photons for this case. The bremsstrahlung contributes about 0.1% to the dose, well below the upper limit obtained by measurement. We conclude that the effect of bremsstrahlung on the detector response can be safely neglected.

III.B. Electron beam angular spread

As pointed out in Sec. II B, the angular spread of the beam is complicated because it does not show cylindrical symmetry. The main feature is a secondary lobe which diverges from the main beam at an angle of up to 0.25°. We investigated the effect of this beam structure by measuring scatter profiles at 20 MeV with no added scattering foil, not only in the horizontal plane, but also in the vertical plane and in the two planes at 45° with respect to the horizontal plane. The maximum difference in $\theta_{1/e}$ for the four angular positions was about 1% with the largest value occurring for the scan at 45° that passed over the secondary lobe.

We also used BEAMnrc to calculate the effect on the scatter distribution of adding a secondary beam at a small angle with respect to the main beam. It predicts a maximum broadening of the scatter distribution of about 0.5%, or about half of the measured value. The effect of the beam divergence is similar in size to the estimated uncertainties on $\theta_{1/e}$ and is significant for only the thinnest foils. The values of

TABLE III. Summary of the measured and calculated characteristic angles $\theta_{1/e}$ for all the scattering foils used in this study. The values in the columns labeled "Dif." were calculated as the ratio of the difference between the calculated and measured values to the measured value. Except for Ti, each distribution is labeled according to the added scattering foil, but all of the scattering material indicated in Fig. 1 is present in each case. In the case of the Ti alloy, the thickness of the beam exit window is included in the stated foil thickness. Not all foils were measured at both energies, and a dash is used to indicate those cases where no data are available.

		13 MeV			20 MeV		
	Thick. (mg/cm^2)	Meas. (deg)	Calc. (deg)	Dif. (%)	Meas. (deg)	Calc. (deg)	Dif. (%)
Be	926	8.143	8.093	−0.6	5.238	5.259	0.4
C	546	7.933	7.600	−4.2	5.132	4.975	−3.1
Al	70.1	4.003	3.956	−1.2	2.653	2.606	−1.8
	140	5.268	5.217	−1.0	3.484	3.434	−1.4
	274	—	—	—	4.777	4.699	−1.6
	414	—	—	—	5.865	5.797	−1.2
Ti alloy	18.21	2.380	2.295	−3.6	1.550	1.510	−2.6
	36.4	3.103	3.016	−2.8	2.032	1.983	−2.4
	54.6	3.712	3.621	−2.5	2.452	2.389	−2.5
	72.8	4.261	4.177	−2.0	2.808	2.747	−2.2
	91.0	4.771	4.668	−2.2	3.140	3.071	−2.2
Cu	43.0	4.219	4.166	−1.3	2.790	2.742	−1.7
	86.4	5.630	5.579	−0.9	3.714	3.669	−1.2
	129.6	6.861	6.752	−1.6	4.493	4.440	−1.2
	174.5	7.956	7.829	−1.6	5.198	5.143	−1.1
Ta	44.3	5.558	5.463	−1.7	—	—	—
	206.3	—	—	—	7.913	7.836	−1.0
Au	31.2	4.878	4.789	−1.8	—	—	—
	54.8	6.329	6.170	−2.5	4.127	4.062	−1.6
	93.7	8.243	8.029	−2.6	—	—	—
	109.5	—	—	—	5.881	5.781	−1.7
	164.2	—	—	—	7.278	7.143	−1.9
	219	—	—	—	8.566	8.373	−2.3

$\theta_{1/e}$ for the two thinnest foils at 20 MeV have been corrected for beam divergence. The effect is sufficiently small for other cases that it can be ignored.

III.C. Residual air in the He gas column

As discussed in Sec. II E, the flow of helium gas was used to slowly displace the air in the Mylar bag. Some scans were repeated as the air was being displaced, and give a measure of the effect of residual air on the scatter distribution. In some other cases, we realized that the measured distribution was still being impacted by residual air mixed with the helium. Because the oxygen concentration was being monitored, the contribution of the residual air to the width of the scatter distribution, $\theta_{1/e}$, could be estimated. The largest correction was 0.3% for one of the Au foils at 20 MeV.

III.D. Measured and calculated scatter distributions

The measured scatter distributions are available in tabular form from the AIP electronic repository.[27] Although the data are labeled by the scattering foil, the scatter distribution includes the effects of the extra material in the beam path. Because the data are intended for testing Monte Carlo codes, and because these codes can easily simulate the additional material, we have not attempted to correct the measured distributions for these effects.

Table III summarizes all of the measured and calculated values of $\theta_{1/e}$. The differences between the calculated and measured values are presented graphically in Fig. 6. In general, EGSnrc predicts scatter distributions that are slightly narrower than measured. The maximum difference is about 4%, but in most cases the differences are smaller than twice the standard uncertainty.

Comparing measured and calculated values of $\theta_{1/e}$ gives a quantitative indication of how well the distributions agree near the central axis. Even if significant differences are noted, one may still consider whether or not the two distributions have the same shape over the whole angular range. If the shapes are the same, one distribution can be mapped onto the other through a simple scaling of the angular variable. The lower panel in Fig. 7 shows the measured and calculated distributions for 13 MeV electrons with no added scattering

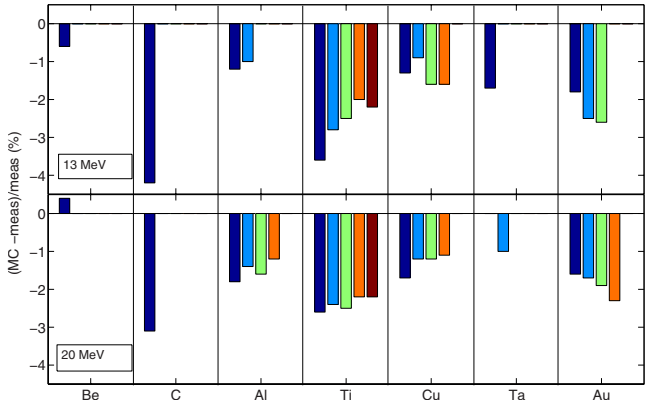

FIG. 6. Graphical summary of the differences between the calculated and measured values of $\theta_{1/e}$ for all scattering foils and both energies. Each bar corresponds to a different foil thickness, the values of which can be obtained from Table III. The standard uncertainty of the length of each bar is about 1%, i.e., one unit on the ordinate, and specific values can be obtained from Table IV.

TABLE IV. Summary of the estimated uncertainties that contribute to the measured value of $\theta_{1/e}$. Essentially all uncertainties are type B (systematic). The contribution of some components, such as the detector resolution, depends on the width of the distribution. The contributions are approximately the same for both 13 and 20 MeV.

	20 MeV window $u_i(\%)$	$\theta_{1/e}\approx 2°$ $u_i(\%)$	$\theta_{1/e}\approx 4°$ $u_i(\%)$	$\theta_{1/e}\approx 8°$ $u_i(\%)$
Beam energy	0.4	0.4	0.4	0.4
Angular spread	0.2	0.2	0.1	0
Beam alignment	0.2	0.1	0.1	0.1
Foil thickness	0.25	0.25	0.25	0.25
Detector resolution	0.3	0.17	0.04	0
Detector response	0.5	0.3	0.2	0.2
Detector positioning	0.3	0.3	0.3	0.3
Repeatability	0.3	0.3	0.3	0.3
Fitting	0.5	0.5	0.5	0.5
Quadratic sum	1.04	0.91	0.85	0.84

foil, plotted as the square of the scattering angle versus the negative logarithm of the normalized fluence. If the distributions were strictly Gaussian, the data points, when plotted this way, would lie on straight lines. If the values of θ^2 of the calculated distribution are scaled by 1.079, then they are close to the values of θ^2 of the measured distribution. The extent of the agreement is shown in more detail in the upper panel of Fig. 7 which gives the ratio of the measured to the calculated values of θ^2, with the calculated values scaled by 1.079.

Note that the calculated data has been interpolated to obtain values along the abscissa that match the measured data. The increased scatter of the data for small values of the abscissa is because of limited precision in determining the scattering angle for values close to the central axis. The splitting of the data into two bands is due to a slight asymmetry in the measured scatter distribution. The approximate constancy of the ratio indicates that the shapes of the measured and calculated distributions are very similar. Furthermore, the scaling factor is in satisfactory agreement with the value of 1.072 that would be predicted using the difference between the measured and calculated values of $\theta_{1/e}$ given in Table III.

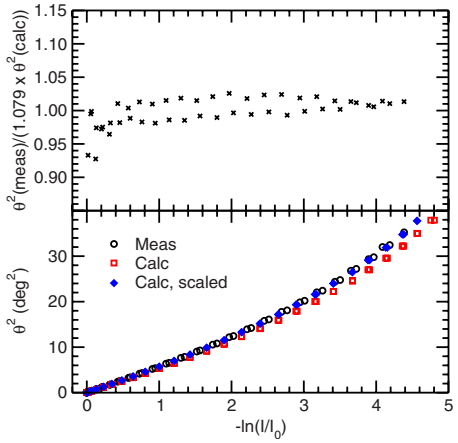

FIG. 7. Comparison of measured and calculated scatter distributions over a large angular range for 13 MeV electrons with no added scattering foil. If the distributions were Gaussian, they would appear as straight lines in the lower panel. The calculated distribution can be made coincident with the measured by multiplying the calculated values of θ^2 by 1.079. The upper panel shows the same data, but presented as the ratio of the measured value of θ^2 to the calculated and scaled value. If the measured and calculated distributions have the same shape they will be related through a scaling of the angular variable and the ratio will be constant.

III.E. Uncertainties

The uncertainties of the measured distributions arise from several sources: the characteristics of the electron beam; the material that scatters the beam; the electron-fluence response of the detector and its spatial resolution; detector positioning; detector and monitor chamber noise and stability; and the fitting of the measured distributions. We examine how each of these sources contributes to the overall uncertainty of the values of $\theta_{1/e}$ and the results are summarized in Table IV. Unless otherwise indicated, the standard uncertainties, corresponding to one standard deviation, are given.

According to the data presented in ICRU 35, the mean-square scattering angle, $\langle\theta^2\rangle$, is closely proportional to $1/E^2$ for all materials, where E is the electron beam energy. The uncertainty of E is 0.4% and thus its contribution to the uncertainty of $\theta_{1/e}$ also will be 0.4%. The beam profile has been shown to be approximately Gaussian with a root-mean-square radius of about 1 mm. A Monte Carlo calculation was carried out to determine how changing the beam diameter would impact the measured distributions. For the sharpest distribution (20 MeV with no added scattering foil) changing the root-mean-square radius from 1 to 2 mm increased $\theta_{1/e}$ by 0.27%. We conclude that the electron beam profile does not contribute significantly to the width of the measured distributions or its uncertainty. The effect of the beam angular spread has been discussed in Sec. III B. It was shown to affect the width of the sharpest distribution by up to 1% and a suitable correction was applied. Assuming that the angular

spread adds quadratically to the intrinsic distribution, the effect decreases rapidly with increasing $\theta_{1/e}$, and is less than 0.25% for a distribution with $\theta_{1/e}$ equal to 3°. The contribution of the angular spread to the uncertainty of $\theta_{1/e}$ is given for representative angles in Table IV. The effect of misalignment between the beam axis and that defined by the detector was discussed in Sec. II G and from that analysis we assign a maximum uncertainty due to beam alignment of 0.2%.

The scattering foils used varied in thickness from about 15 to 5000 μm. For the thicker foils, the linear thickness of the foil can be measured at several points, but this does not address the possibility of density variations throughout the foil. A direct measurement of the linear thickness of the thin foils was not possible so the mass thickness was obtained from area and weight measurements. In this approach, the foil thickness is assumed to be uniform. Although the mass of a thin foil can be measured with high precision, the area presents more of a challenge because of possible edge effects. Foil nonuniformities were assessed from repeated measurements of the same distribution but with different foils and from variability in the mass thickness measured from different samples cut from the same sheet. We estimate that the standard uncertainty of the mass thickness is about 0.5% for all materials except pyrolytic graphite for which we assign an uncertainty of 1%. Because $\langle\theta^2\rangle$ is proportional to the mass thickness of the foil, these uncertainties contribute 0.25% and 0.5% to the uncertainty of $\theta_{l/e}$. Of the extra material in the beam, the monitor chamber makes the largest contribution to the uncertainty. Using samples from a broken chamber we determined that each foil consists of Mylar with a mass thickness of 1.62 mg/cm^2 covered with a layer of carbon-based material 1.01 mg/cm^2 thick. We carried out auxiliary measurements in which the monitor chamber was removed and a temporary monitor mounted downstream of the scanning detector was used. The effect of removing the chamber on the sharpest scatter distribution was measured and compared to the value calculated using EGSnrc. For the simulation, the chamber was modeled as a single layer of Mylar with a mass thickness equal to six times the measured mass thickness of a single foil. The results were consistent, indicating that the monitor chamber can be considered to be Mylar with a total mass thickness of 15.78 mg/cm^2 with an uncertainty of 0.5%. Because the mass thickness of the chamber was always less than one third of the total mass thickness of all the scattering material, its contribution to the mass thickness uncertainty was less than 0.2%.

Detector response issues were discussed in Sec. III A. The finite detector size leads to resolution broadening of the narrowest distributions by about 0.3% but the effect is negligible for the broadest distributions. Issues related to ion recombination effects for ionization chambers or dose rate effects for diodes may contribute an additional uncertainty of 0.5% to $\theta_{l/e}$.

Uncertainties in the detector position with respect to the beam exit window contribute to uncertainties in the measured angle and may be as large as 0.3%. An indication of the stability of the detector to monitor ratio is that the day-to-day repeatability on $\theta_{l/e}$ was typically better than 0.4%.

The fitting procedure used for extracting $\theta_{l/e}$ is described in Sec. II G. The fit is somewhat sensitive to the number of data points used and how they are distributed. The uncertainty of either the measured or calculated value of $\theta_{l/e}$ is about 0.5% due to the fitting procedure. The uncertainty of the difference may be somewhat smaller because the same protocol was used for all distributions, either measured or calculated.

Sufficient Monte Carlo histories were run so that statistical uncertainties make no significant contribution to the calculated values of $\theta_{l/e}$. Because the primary objective of this study was to obtain measured scatter distributions, we have not attempted to estimate systematic uncertainties due to the Monte Carlo algorithms.

IV. CONCLUSIONS

The electron scattering measurements of Hanson *et al.*[6] produced important benchmark data that has been used to test Monte Carlo codes used for medical physics. Because they used scattering foils mounted in a vacuum chamber, there was no additional scattering material to perturb the measured distributions. They also claim that the angular spread of their incident electron beam was sufficiently small that it could be neglected and their apparatus permitted them to obtain absolute yields. On the other hand, the complexity of an evacuated scattering chamber makes it difficult to do a survey of a wide range of scattering materials.

This work shows that it is possible to obtain high-precision scattering data without the necessity of a vacuum chamber. We take advantage of the fact that modern Monte Carlo codes can simulate the full scatter geometry so there is no reason to obtain the scatter distribution that would be produced by the scattering foil on its own. The scatter distributions reported here and in the EPAPS supplement[27] include all of the scatter material in the beam path. The distributions were measured in a plane at right angles to the beam direction and in the EPAPS supplement the results are reported in terms of the detector position. In the results presented here, the off-axis angle is used to describe the distributions.

Unlike the Hanson *et al.* data, our fluence measurements are not absolute. We have the capability of measuring the incident beam current absolutely but would need to operate at significantly higher beam currents to achieve adequate precision. Higher electron fluence rates exacerbate problems due to dose rates effects for diodes and ion recombination for ionization chambers and would likely mean that a different type of detector would be needed. Vilches *et al.*[9,10] have shown that the electron scatter distribution can have a significant effect on the shape of the depth-dose curve and that differences between different codes are often obscured by first normalizing to the peak of the depth-dose curve. Absolute measurements of the depth-dose curve per incident elec-

tron would be easier than absolute measurements of the scatter distribution and would serve to test the effects identified by Vilches *et al.*

We found (Fig. 7) that a simple scaling of the angular variable leads to satisfactory agreement between our measured and calculated distributions for all angles, indicating that they have the same shape.

We used the angle $\theta_{1/e}$ where the fluence has fallen to $1/e$ of its value on the central axis, to characterize the measured and calculated distributions. Figure 6 shows that EGSnrc predicts distributions that are slightly narrower than measured, although in many cases the differences are less than twice the standard uncertainty of the measured value. Vilches *et al.*[8,9] show that some popular Monte Carlo codes lead to differences with the Hanson *et al.* data of more than 20%. It would be expected that these codes will show similar differences with the new data presented here.

ACKNOWLEDGMENTS

David Marchington provided valuable technical assistance during the course of this work, including the design and construction of the helium bag and the holder for the scattering foils. He and Matt Kosaki were critical in keeping the accelerator running. Iwan Kawrakow performed some preliminary Monte Carlo calculations of scatter distributions. Blake Walters and Ernesto Mainegra-Hing helped with the EGSnrc and BEAMnrc Monte Carlo codes. Dave Rogers provided useful comments on an early draft of the article. Financial assistance was provided by the National Institutes of Health Grant No. R01 CA104777.

APPENDIX: SUMMARY OF MEASUREMENT GEOMETRY

Each component of the scatter geometry has been discussed in the text. This appendix provides a summary that may be helpful in constructing a model for use in Monte Carlo simulations. We also describe the approximations used in our BEAMnrc model. All axial positions are given with respect to the beam exit window.

Beam window: The beam window has a diameter of 3.8 cm and is composed of Ti alloy 0.0412 mm thick. The alloy composition by weight is 90% Ti, 6% Al, and 4% V. The radius of the window was taken to be 3 cm for the BEAMnrc simulation.

Scattering foil position: The thickness of most scattering foils was negligible compared to the overall dimensions of the scatter geometry, and the upstream surface of the foil was 28 mm from the exit window. The thicker Be and C foils were positioned with their upstream edges at 25 mm. For the BEAMnrc model, the upstream surface of every foil was set to 28 mm from the exit window.

Scattering foils: The scattering foil characteristics are given in Tables I and III. In most cases the diameter of the foil was restricted to 2 cm. However, the diameter of the graphite and beryllium foils was 5 cm. For the BEAMnrc simulation, the radius of every foil was set to 1 cm.

Monitor chamber position: The center of the monitor chamber was 50 mm from the exit window.

Monitor chamber: The monitor chamber is composed of six foils and the distance between the first and last is 6 mm. The foils are supported in a structure with a circular opening with a diameter of 9 cm. According to the manufacturer, each foil is composed of Mylar (12 μm thick, density 1.40 g/cm^3) coated with graphite-based conductive ink (12 μm thick, density 1.00 g/cm^3). We do not have detailed information on the nature of the conducting ink, but we measured the mass thicknesses of the Mylar and ink to be 1.62 and 1.01 mg/cm^2, respectively. For the BEAMnrc model, the chamber was taken to be a single Mylar foil with a thickness of 0.1127 mm and a density of 1.40 g/cm^3, positioned 50 mm from the exit window.

Helium bag: All the walls were constructed of aluminized Mylar. The Mylar and aluminum was 25 and 24 nm thick, respectively. The diameter of the bag was 46 cm. The bag was 110 cm long and the upstream window of the bag was 6.5 cm from the beam exit window. The aluminum on the Mylar was not included in the BEAMnrc model and the outer diameter of the bag set the maximum diameter of the geometry. That is, once a particle passed through the sidewall of the bag it was lost from the simulation. Note that the dimensional information related to the helium bag is approximate because the walls are not perfect planes when the bag is inflated.

Detector: The detector, either a diode or ionization chamber, was placed so that the centre of its sensitive volume was 118.2 cm from the beam exit window.

[a]Author to whom correspondence should be addressed. Telephone: 613 993-9352, ext. 233; Fax: 613 952 9865. Electronic mail: carl.ross@nrc-cnrc.gc.ca
[b]Also at: Ottawa Carleton Institute of Physics, Carleton University, 1125 Colonel By Drive, Ottawa, Ontario K1S 5B6, Canada.

[1]P. Mayles, A. Nahum, and J. C. Rosenwald, *Handbook of Radiotherapy Physics: Theory and Practice* (CRC Press, Boca Raton, FL, 2007).
[2]M. J. Berger, "Monte Carlo calculation of the penetration and diffusion of fast charged particles," in *Methods in Computational Physics*, edited by B. Alder, S. Fernbach, and M. Rotenberg (Academic, New York, 1963), pp. 135–215.
[3]ICRU, *Stopping Powers for Electrons and Positrons*, ICRU Report 37 (ICRU, Bethesda, MD, 1984).
[4]ICRU, *Radiation Dosimetry: Electron Beams With Energies Between 1 and* 50 MeV, ICRU Report 35 (ICRU, Bethesda, MD, 1984).
[5]G. Molière, "Theorie der streuung schneller geladener Teilchen II: Mehrfach und vielfachstreuung," Z. Naturforsch. A **3A**, 78–97 (1948).
[6]A. O. Hanson, L. H. Lanzl, E. M. Lyman, and M. B. Scott, "Measurement of multiple scattering of 15.7 MeV electrons," Phys. Rev. **84**, 634–637 (1951).
[7]X. A. Li and D. W. O. Rogers, "Electron mass scattering powers: Monte Carlo and analytical calculations," Med. Phys. **22**, 531–541 (1995).
[8]M. Vilches, S. García-Pareja, R. Guerrero, M. Anguiano, and A. M. Lallena, "Monte Carlo simulation of the electron transport through thin slabs: A comparative study of PENELOPE, GEANT3, GEANT4, EGSnrc and MCNPX," Nucl. Instrum. Methods Phys. Res. B **254**, 219–230 (2007).
[9]M. Vilches, S. Garcia-Pareja, R. Guerrero, M. Anguiano, and A. M. Lallena, "Effect of electron transport through thin slabs on the simulation of linear electron accelerators of use in therapy: A comparative study of various Monte Carlo codes," Nucl. Instrum. Methods Phys. Res. A **580**, 153–156 (2007).
[10]M. Vilches, S. García-Pareja, R. Guerrero, M. Anguiano, and A. M. Lallena, "Effect of the multiple scattering of electrons in Monte Carlo simulation of Linacs," Radiother. Oncol. **86**, 104–108 (2008).

[11]L. A. Kulchitsky and G. D. Latyshev, "The multiple scattering of fast electrons," Phys. Rev. **61**, 254–265 (1942).
[12]F. F. Heymann and R. E. Jennings, "The multiple scattering of 4.5 MeV electrons," Proc. R. Soc. London, Ser. A **234**, 116–124 (1956).
[13]V. P. Kovalev, V. P. Kharin, V. V. Gordeev, and V. I. Isaev, "Angular distributions of electrons with initial energies of 12–25 MeV behind tungsten, cadmium and copper barriers," At. Energy **33**, 1088–1090 (1972).
[14]W. R. Nelson, H. Hirayama, and D. W. O. Rogers, The EGS4 Code System, SLAC-265, Stanford Linear Accelerator Laboratory, Stanford, CA, 1985.
[15]I. Kawrakow, "Accurate condensed history Monte Carlo simulation of electron transport. I. EGSnrc, the new EGS4 version," Med. Phys. **27**, 485–498 (2000).
[16]H. A. Bethe, "Molière's theory of multiple scattering," Phys. Rev. **89**, 1256–1266 (1953).
[17]A. F. Bielajew, "Plural and multiple small-angle scattering from a screened Rutherford cross section," Nucl. Instrum. Methods Phys. Res. B **86**, 257–269 (1994).
[18]J. M. Fernández-Varea, R. Mayol, J. Baró, and F. Salvat, "On the theory and simulation of multiple elastic scattering of electrons," Nucl. Instrum. Methods Phys. Res. B **73**, 447–473 (1993).
[19]P. Andreo, J. Medin, and A. F. Bielajew, "Constraints of the multiple-scattering theory of Molière in Monte Carlo simulations of the transport of charged particles," Med. Phys. **20**, 1315–1325 (1993).
[20]I. Kawrakow and A. F. Bielajew, "On the representation of electron multiple elastic-scattering distributions for Monte Carlo calculations," Nucl. Instrum. Methods Phys. Res. B **134**, 325–336 (1998).
[21]B. A. Faddegon, J. Perl, and M. Asai, "Monte Carlo simulation of large electron fields," Phys. Med. Biol. **53**, 1497–1510 (2008).
[22]M. S. MacPherson and C. K. Ross, A Magnetic Spectrometer for Electron Energy Calibration, NRC Report PIRS-0617, National Research Council, Ottawa, 1998.
[23]I. Kawrakow and D. W. O. Rogers, The EGSnrc Code System: Monte Carlo Simulation of Electron and Photon Transport, NRC Report PIRS-701, National Research Council, Ottawa, http://www.irs.inms.nrc.ca/EGSnrc/pirs701.pdf, 2006.
[24]D. W. O. Rogers, B. A. Faddegon, G. X. Ding, C.-M. Ma, and J. Wei, "BEAM: A Monte Carlo code to simulate radiotherapy treatment units," Med. Phys. **22**, 503–524 (1995).
[25]I. Kawrakow, EGSnrc C++ Class Library, NRC Report PIRS-898, National Research Council, Ottawa, http://www.irs.inms.nrc.ca/EGSnrc/pirs898/index.html, 2005.
[26]C. M. Ma and D. W. O. Rogers, BEAMDP Users Manual, NRC Report PIRS-509, National Research Council, Ottawa, http://www.irs.inms.nrc.ca/BEAM/user_manuals/beamdp_um/beamdp_um.html, 2007.
[27]See EPAPS Document No. E-MPHYA6-35-034809 for several of the measured scatter distributions from which the results presented in this paper are derived. For more information on EPAPS, see http://www.aip.org/pubservs/epaps.html.
[28]US National Institutes of Health, http://rsb.info.nih.gov/ij.